

THE INTERPRETATION OF THE MULTI-WAVELENGTH AFTERGLOW EMISSION OF SHORT GRB 140903A

SHUAI ZHANG^{1,2}, ZHI-PING JIN¹, YUAN-ZHU WANG^{1,2}, AND DA-MING WEI¹

¹ Key Laboratory of Dark Matter and Space Astronomy, Purple Mountain Observatory, Chinese Academy of Sciences, Nanjing, 210008, China. and

² University of Chinese Academy of Sciences, Yuquan Road 19, Beijing, 100049, China.

Draft version November 8, 2018

ABSTRACT

GRB 140903A, a short duration γ -ray burst (SGRB) detected by *Swift*, is characterized by its long-lasting radio emission among SGRBs. In addition to the $\sim 10^6$ s radio afterglow emission, the afterglow of GRB 140903A displays a plateau from 10^3 s to 7×10^3 s in the X-rays. In this work, we attribute the X-ray plateau to the energy injection into the decelerating blast wave and then model the later radio/optical/X-ray afterglow emission within the standard fireball afterglow model. The afterglow emission has been well reproduced with reasonable physical parameters, including a jet half-opening angle ~ 0.05 . We also compare the physical properties of SGRBs with and without radio afterglow detections and find that nearby SGRBs are brighter and easier to be detected in radio. Such a phenomena has been interpreted within the afterglow model.

Subject headings: gamma-ray burst: general-gamma-ray burst: individual (GRB 140903A)-ISM: jets and outflows

1. INTRODUCTION

Gamma-ray bursts (GRBs) are the most energetic flashes of soft γ -ray from the deep universe. Based on their duration distribution, GRBs can be generally divided into two groups, including the so-called short GRBs (SGRBs; the duration is shorter than 2 second) and long GRBs. (Kouveliotou et al. 1993). Usually the long GRBs are associated with bright supernovae and thus should be from massive star collapse (Woosley & Bloom 2006). The SGRBs, however, are expected to be from neutron star mergers (including both the double neutron star mergers and neutron star-black hole mergers) (Eichler et al. 1989). The compact object merger origin of SGRBs has been strongly supported by their afterglow and host galaxy observations (Berger 2014; Fong et al. 2015) and the identification of Li-Paczynski macronovae (Li & Paczyński 1998; Kasen et al. 2013) in SGRB 130603B (Tanvir et al. 2013; Berger et al. 2013), long-short GRB 060614 (Yang et al. 2015; Jin et al. 2015) and SGRB 050709 (Jin et al. 2016). SGRBs are hence widely believed to be promising gravitational wave (GW) sources and important sites of generating heavy elements (Eichler et al. 1989; Jin et al. 2016) and the SGRB/GW association is expected to be reliably established in the advanced LIGO/Virgo era (see Li et al. (2016) and the references therein). The observations of SGRBs have attracted wider and wider attention and the modeling of the afterglow can provide additional information. For instance the derivation of the half-opening angle of the SGRB ejecta is important for estimating the detection prospect of GW emission from neutron star mergers by advanced LIGO/Virgo network (Berger 2014) and the afterglow modeling may reveal the nature of the central engine of short GRBs.

In this work we focus on GRB 140903A, a short burst characterized by its long-lasting radio emission.

Before the detection of this event, there had been just three short GRBs with radio afterglow and all had been detected by The Jansky Very Large Array (VLA), including GRB 050724A (Berger et al. 2005; Panaitescu 2006), GRB 051221A (Soderberg et al. 2006) and GRB 130603B (Fong et al. 2014). Among the limited sample, GRB 140903A has the longest radio afterglow detection ($\sim 10^6$ s). In addition to the long-lasting radio afterglow emission, the afterglow of GRB 140903A displays a plateau from 10^3 s to 7×10^3 s in the X-rays. The main purpose of this work is to interpret these features. We also carry out the statistical study to examine why the radio afterglow detection of SGRBs are so rare.

Recently Troja et al. (2016) reported their observing result of GRB 140903A. They monitored the X-ray afterglow up to 15 days with *Chandra*. Together with the optical and radio afterglow data, they found an achromatic jet break at about 1 day after the burst. They discussed the nature of the GRB progenitor system and concluded that this event likely originated from a compact binary merger. An off-axis jet model was used to interpret the multi-band afterglow. In this work we carry out an independent analysis in the on-axis jet scenario.

2. THE AFTERGLOW EMISSION OF SGRB 140903A AND THE INTERPRETATION

2.1. The afterglow data

At 15:00:30 UT on 2014 Oct 03, GRB 140903A triggered the Burst Alert Telescope (BAT) onboard the *Swift* satellite (Cummings et al. 2014). Its duration T_{90} (15-350 keV) is 0.30 ± 0.03 second. The time-averaged spectrum between $T_0 - 0.01$ to $T_0 + 0.35$ second is best fitted by a simple power-law model, with a photon index 1.99 ± 0.12 (Palmer et al. 2014).

Swift XRT began to observe the position of GRB 140903A at about 59 seconds after the BAT trigger (Kennea & Cummings 2014) and detected the afterglow

(DePasquale et al. 2014). The X-ray afterglow decay firstly ($\alpha \sim 0.2$) before 1000 seconds and then followed by a plateau with a flux $\sim 10^{-11} \text{ erg cm}^{-2} \text{ s}^{-1}$ until about 10^4 s and then turned to a more rapid decay (DePasquale et al. 2014; Troja et al. 2016). *Chandra* took two epochs of observations of the afterglow at about 3 and 21 days after the burst and both detected the source (Sakamoto et al. 2014; Troja et al. 2016). Compared them with the *Swift* XRT data, there was a jet break at about 1 days (Troja et al. 2016).

The afterglow of GRB 140903 had been observed by many ground-based telescopes. Among them, the 4.3m Discovery Channel Telescope (Capone et al. 2014), the robotic Palomar 60 inch telescope (Cenko & Perley 2014), the Gemini-North telescope (Cucchiara et al. 2014; Levan et al. 2014), the Pan STARRS survey telescope (Fruchter 2014), the Faulkes Telescope North (Dichiara et al. 2014) and the Nordic Optical Telescope (Xu et al. 2014) detected the optical counterpart of the X-ray afterglow. Gemini GMOS observed the source in spectroscopic mode at about 14.6 hours after the burst, and the redshift $z = 0.351$ was determined by identifying the $H\beta$ and OIII emission lines and the NaI absorption line (Cucchiara et al. 2014). This was confirmed by later spectroscopy of the host galaxy by GTC, which detected a $H\alpha$ line at the same redshift (Troja et al. 2016). The radio afterglow of 6.1 GHz and 9.8 GHz was also detected by the Very Large Array (VLA) at about 10 hours after the trigger of BAT (Fong 2014), it was still detectable until 10^6 s. The radio flux rise firstly and then decay, the peak flux density is $\sim 200 \mu\text{Jy}$ at about 2×10^5 s (Troja et al. 2016). The Giant Metrewave Radio Telescope (GMRT) also detected the radio emission (Nayana & Poonam 2014). In this work we give an interpretation of these observational features within the framework of external forward shock model with energy injection.

2.2. X-ray afterglow flat segment due to the energy injection

Flat segment of X-ray afterglow has been detected in a good fraction of long GRB afterglows (Nousek et al. 2006; Zhang et al. 2006) and some SGRB afterglows (Burrows et al. 2006). Such a kind of phenomena has been widely interpreted as the energy injection from the prolonged activity of the central engine (Zhang et al. 2006; Fan & Xu 2006). However, sometimes the optical afterglow emission can not be interpreted self-consistently within such a scenario (Fan & Piran 2006; Liang et al. 2007; Panaitescu et al. 2006).

The energy injection can be written generally as (Cohen & Piran 1999; Zhang & Mészáros 2001; Zhang et al. 2006):

$$\frac{dE}{dt} = A(1+z)^{-1} \left(\frac{t}{t_0}\right)^{-q}, \quad t_i < t < t_f \quad (1)$$

where t_i and t_f represent the start and end time of energy injection. At the time of t_c (when the amount of injected energy equals to the initial kinetic energy in the outflow) the dynamical evolution of the GRB ejecta is changed significantly, i.e. $\int_{t_i}^{t_c} (dE/dt) dt \sim E_k$, where E_k is the kinetic energy of the outflow. Then we get $At_0^q(t_c^{1-q} - t_i^{1-q}) \sim (1+z)(1-q)E_k$.

From observations we know that $\nu_c(t_d = 1) \gtrsim 10$ keV for SGRB 140903A. In this case, the X-ray flat plateau decline as $\alpha = \frac{(2p-4)+(p+2)q}{4}$ (Zhang et al. 2006). For typical value of $p \sim 2.2 - 2.5$, the X-ray flat segment of SGRB 140903A is in agreement with the case of $q \sim 0$, i.e., the central engine is a pulsar-like compact object. Similar conclusions have been drawn for example for SGRB 151221A (Fan & Xu 2006). In the case of long GRBs, please see Dai & Lu (1998) and Zhang & Mészáros (2001). For $q \sim 0$, we have $A \sim \frac{(1+z)E_k}{t_c - t_i}$.

We consider the energy injection (Pacini 1967; Gunn & Ostriker 1969) as:

$$\frac{dE}{dt} \approx \frac{6.2 \times 10^{47}}{1+z} \text{ erg s}^{-1} B_{\perp,14}^2 R_{s,6}^6 \Omega_4^4 \left[1 + \frac{t}{(1+z)T_o}\right]^{-2}, \quad (2)$$

where B_{\perp} and R_s are the component of the dipole magnetic field strength perpendicular to the rotation axis and radius of the magnetar respectively, Ω is the initial angular frequency of rotation. The initial spin-down time-scale in the rest frame is:

$$T_o \approx 1.6 \times 10^5 \text{ s } B_{\perp,14}^{-2} \Omega_4^{-2} I_{45} R_{s,6}^{-6} \quad (3)$$

and in which $I \sim 10^{45}$ is the typical moment of inertia of magnetar. Here and after, we adopted the convention $Q_x = Q/10^x$ in cgs units.

When $t \ll (1+z)T_o$, the energy injection rate is a constant, so with our magnetar model one requires $q \sim 0$ for $t_c < (1+z)T_o$, we can derive:

$$A \sim \frac{(1+z)E_k}{t_c - t_i} \sim 6.2 \times 10^{47} \text{ erg s}^{-1} B_{\perp,14}^2 R_{s,6}^6 \Omega_4^4 \quad (4)$$

For $t > (1+z)T_o$, the energy injection rate drops rapidly. So we have

$$t_f \sim (1+z)T_o \sim 1.6 \times 10^5 \text{ s } (1+z) B_{\perp,14}^{-2} \Omega_4^{-2} I_{45} R_{s,6}^{-6} \quad (5)$$

The total energy injection can be estimated as $E_{inj} = AT_o$, so together with (3) and (4) we can get $E_{inj} = t_f E_k / (t_c - t_i) \sim 10^{53} \text{ erg } I_{45} \Omega_4^2$. Then the ratio of total injected energy to initial kinetic energy is:

$$\frac{E_{inj}}{E_k} \sim \frac{10^{53} \text{ erg } I_{45} \Omega_4^2}{E_k} \quad (6)$$

From the X-ray afterglow of GRB 140903A, we can infer that the energy injection begins important during about 1000 \sim 2000 s and ends at about 7000 s, so we estimate $t_c - t_i \sim 1000$ s and $t_f \sim 7000$ s. So $E_{inj}/E_k \sim t_f/(t_c - t_i) \sim 7$. Substituting this into equation (6) we get $E_k \sim 1.4 \times 10^{52} \text{ erg } I_{45} \Omega_4^2$. Then by equation (4) we obtain $A \sim 1.9 \times 10^{49} \text{ erg } I_{45} \Omega_4^2$, here $z = 0.351$ is adopted. By assuming typical values of $I_{45} = 1$ and $\Omega_4 = 0.58$ (Shapiro & Teukolsky 1983), we can estimate $E_k \sim 4.7 \times 10^{51} \text{ erg}$ and $A \sim 6.4 \times 10^{48} \text{ erg s}^{-1}$.

We can also constrain the ellipticity $\epsilon \equiv \frac{a-b}{(a+b)/2}$ of the magnetar if we assume gravitational wave radiation is not important. The spin-down time-scale of gravitational wave radiation can be estimated as $\tau_{gw} \sim 3 \times 10^{-3} \epsilon^{-2} I_{45}^{-1} \Omega_4^{-4} \text{ s}$ (Shapiro & Teukolsky 1983). From $\tau_{gw} > t_f \sim 7000$ s we can get $\epsilon < 6.5 \times 10^{-4} I_{45}^{-1/2} \Omega_4^{-2}$.

2.3. Analytical estimate of forward shock physical parameters

The forward shock emission from GRB outflow can be parameterized as (e.g., Piran 1999; Yost et al. 2003; Fan & Piran 2006):

$$F_{\nu, \max} = 6.6 \text{ mJy} \left(\frac{1+z}{2} \right) D_{L, 28.34}^{-2} \epsilon_{B, -2}^{1/2} E_{k, 53} n_0^{1/2}, \quad (10)$$

$$\nu_m = 2.4 \times 10^{16} \text{ Hz} E_{k, 53}^{1/2} \epsilon_{B, -2}^{1/2} \epsilon_{e, -1}^2 C_p^2 \left(\frac{1+z}{2} \right)^{1/2} t_{d, -3}^{-3/2}, \quad (11)$$

$$\nu_c = 4.4 \times 10^{16} \text{ Hz} E_{k, 53}^{-1/2} \epsilon_{B, -2}^{-3/2} n_0^{-1} \left(\frac{1+z}{2} \right)^{-1/2} t_{d, -3}^{-1/2} \frac{1}{(1+Y)}, \quad (12)$$

where $C_p \equiv 13(p-2)/[3(p-1)]$, ϵ_e (ϵ_B) is the fraction of energy of shocked electrons (magnetic field), the Compton parameter $Y \sim (-1 + \sqrt{1 + 4\eta\epsilon_e/\epsilon_B})/2$, $\eta \sim \min\{1, (\nu_m/\bar{\nu}_c)^{(p-2)/2}\}$ and $\bar{\nu}_c = (1+Y)^2\nu_c$.

Equations (7) to (9) can be transferred to (Zhang et al. 2015):

$$\epsilon_{B, -2}^{1/2} E_{k, 53} n_0^{1/2} \approx a, \quad (10)$$

$$E_{k, 53}^{1/2} \epsilon_{B, -2}^{1/2} \epsilon_{e, -1}^2 \approx b, \quad (11)$$

$$E_{k, 53}^{-1/2} \epsilon_{B, -2}^{-3/2} n_0^{-1} (1+Y)^{-2} \approx c. \quad (12)$$

where:

$$a = \frac{1}{6.6} \text{ mJy}^{-1} F_{\nu, \max} D_{L, 28.34}^2 \left(\frac{1+z}{2} \right)^{-1} \quad (13)$$

$$b = \frac{1}{2.4} \times 10^{-16} \text{ Hz}^{-1} \nu_m C_p^{-2} \left(\frac{1+z}{2} \right)^{-1/2} t_{d, -3}^{3/2} \quad (14)$$

$$c = \frac{1}{4.4} \times 10^{-16} \text{ Hz}^{-1} \nu_c \left(\frac{1+z}{2} \right)^{1/2} t_{d, -3}^{1/2} \quad (15)$$

For observations we know that $z = 0.351$, $p \approx 2.45$, $F_{\nu, \max} \approx 180 \mu\text{Jy}$, $\nu_m(t_d = 2.5) = 37 \text{ GHz}$ (Troja et al. 2016) and $\nu_c(t_d = 1) \gtrsim 10 \text{ keV}$. Then we can solve equations (10) to (12) numerically to obtain the values of ϵ_B , ϵ_e and E_k as a functions of n_0 , which are shown in Fig. 1. Since we only know the lower-limit of ν_c , we can only obtain the upper-limit of ϵ_B and lower limits of ϵ_e and E_k for a fixed value of n_0 . For example, when $n_0 = 0.002$, we have $\epsilon_B \lesssim 0.03$, $\epsilon_e \gtrsim 0.06$ and $E_k \gtrsim 3.4 \times 10^{51} \text{ erg}$. Usually, $\max\{\epsilon_e, \epsilon_B\} \leq 1/3$ (the equipartition assumption) is required and we need $n_0 < 0.08$. Interestingly, this is in agreement with the expectation that the compact object mergers usually take place in lower density regions.

2.4. Numerical fit to the data

We fitted the multi-band afterglow numerically, the code was introduced in Fan & Piran (2006). If we don't consider the optical extinction, the radio, i -band and X-ray data can be fitted well but r -band is not acceptable (the reduced total chi-square is $\chi^2/dof \sim 3.05$ while r -band contribute almost half of it.), therefore extinction must be considered. Troja et al. studied the afterglow spectral energy distribution of GRB 140903A and gave the Galactic extinction $E_{B-V} \approx 0.03$ and an intrinsic extinction $E_{B-V} \approx 0.15$ (Troja et al. 2016). Assuming the host extinction model is the same as the Galactic, we can get the optical extinction $A_r \approx 0.68$ and $A_i \approx 0.5$.

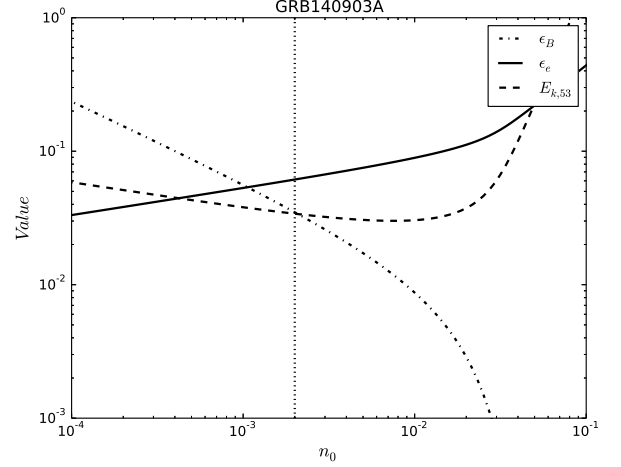


FIG. 1.— Numerical solutions of equations of (10) to (12) as functions of n_0 under assumption of $\nu_c(t_d = 1) \sim 10 \text{ keV}$. The vertical dotted line shows the location of $n_0 = 0.002$. The dot-dashed, solid and dashed lines represent the constraints on ϵ_B , ϵ_e and E_k , respectively.

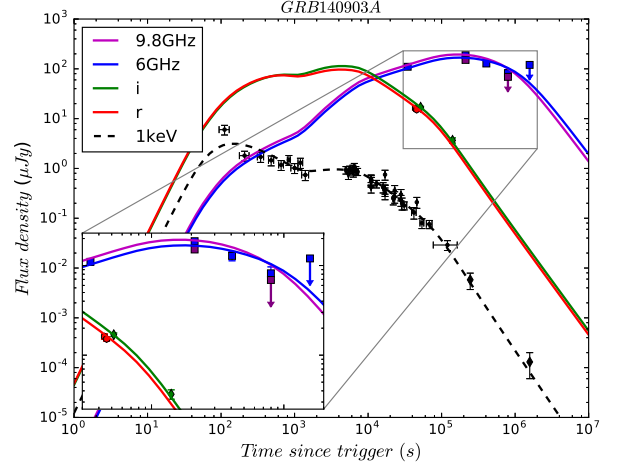


FIG. 2.— Fit of the multi-band afterglow light-curve. Black, red, green, blue and purple represent X-ray (1keV), r , i , 6GHz and 9.8GHz bands respectively. The inset shows the fit of optical and radio observations.

Considering this extinction, we can fit the radio, optical and X-ray light curves well. We use the scenario of a normal expanding jet with a later energy injection. The numerical results are presented in Fig.2, we found this set of fitting parameters (ϵ_e , ϵ_B , p , n_0 , $E_{k, 51}$, θ_j , t_i , t_f , A) $\sim (0.06, 0.01, 2.45, 0.002, 5, 0.05, 1000, 7000, 6 \times 10^{48})$ can reasonably fit the data, where θ_j is the half-opening angle of the GRB outflow. Due to the lack of afterglow data in the early time, the only constraint on the initial Lorentz factor is $\Gamma_0 \geq 200$, and we took 200 in the fit. The values of $E_{k, 51}$, t_i , t_f and A are consistent with previous analytical results. The reduced chi-square is $\chi^2/dof \sim 1.3$.

In our fit (see Fig. 2), the X-ray afterglow first decay before $1 \times 10^3 \text{ s}$ and followed by a continuous energy

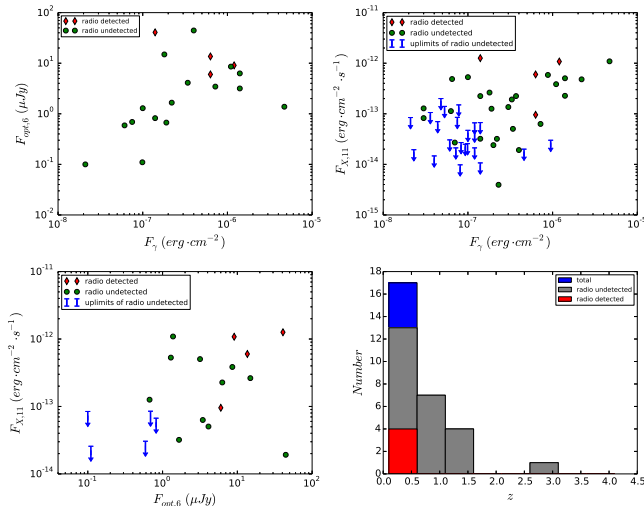


FIG. 3.— *Upper left:* Relation between $F_{\text{opt},6}$ and F_{γ} . *Upper right:* Relation between $F_{X,11}$ and F_{γ} . *Lower left:* Relation between $F_{X,11}$ and $F_{\text{opt},6}$. *Lower right:* Distribution of redshift. Optical and X bands flux densities are observed at 6 and 11 hours after bursts. Green dots and blue upper-limits represent GRBs without radio afterglow detections and red dots represent GRBs with radio afterglow detections.

injection till 7×10^3 s and then turn to a normal decay. At about 1×10^5 s a jet break appeared.

In a previous work, Zhu et al. (2015) have studied another short GRB 130912A which also has a long-lasting optical plateau. However, in that case, the plateau phase can be explained without an energy injection. Here, GRB 140903A has a longer-lasting X-ray plateau and this could be explained by energy injection from 10^3 s to 7×10^3 s.

Troja et al. (2016) got a different set of physical parameters (ϵ_e , ϵ_B , n_0 , $E_{k,\text{iso}}$, θ_j) $\sim (0.14_{-0.06}^{+0.19}, 2.1_{-1.4}^{+3.6} \times 10^{-4}, 0.032_{-0.026}^{+0.14}, 4.3_{-2.0}^{+1.2} \times 10^{52}, 0.090 \pm 0.012$ rad) and an observing angle of $\theta_{\text{obs}} \sim 0.055$ rad. This is natural since we use the energy injection model which is different from their off-axis jet model. We note that the difference in density may explain most of the differences in the physical parameters. However, one should note that in our energy injection model, the total kinetic energy at the end of energy injection is $\sim 4.1 \times 10^{52}$ erg, which is consistent with that of Troja et al. (2016).

3. STATISTICAL STUDY

Except GRB140903A there are only three SGRBs whose radio afterglows have been detected. The properties of those SGRBs have been summarised by Berger (2014). Although the sample is small, we still can do some primary statistics work in purpose of finding what is the difference between SGRBs with and without radio afterglow detections.

Berger (2014) described a sample of 70 SGRBs events with fluence measurements in 15–150 keV (F_{γ}), 28(23) of the 70 events have flux of 0.3–10 keV measurements (up limits) at 11 hours postburst ($F_{X,11}$) and 28 of 70 events have measured redshifts(z).

Together with GRB 140903A which have measured all the F_{γ} (Palmer et al. 2014), $F_{X,11}$ and z (Cucchiara et al. 2014), the total sample consists 71

SGRB events. 13 of 71 events have optical afterglow (Fong et al. 2015) data which can be fitted by broken power law. Then we can get optical flux density at 6 hours postburst ($F_{\text{opt},6}$).

Fig.3 shows the relations between fluence and flux (densities) of different bands and distribution of redshifts. We can see that in the three panel at the front, GRBs with radio afterglow detection generally locate in the upper right side and in the last panel they all gather at lower redshift region. This is natural since usually the “nearby” events are brighter and easier to be detected (in radio and also other bands).

In order to compare the intrinsic properties of the SGRBs with and without radio afterglow detection, we compare the distributions of F_{γ} , $F_{X,11}$, $F_{\text{opt},6}$ and the corresponding energy (E_{γ}) and luminosity ($L_{X,11}$ and $L_{\text{opt},6}$) in Fig.4. Those SGRBs with radio afterglow detections have higher values of F_{γ} , $F_{X,11}$, $F_{\text{opt},6}$ but normal E_{γ} , $L_{X,11}$ and $L_{\text{opt},6}$. We also note that the radio observations are consistent with emission from the forward shock. This means that nearer and brighter SGRBs are more likely to have detectable radio afterglow emission. It is a natural consequence of the limited sensitivity of radio facilities and is consistent with the conclusion made by Chandra & Frail (2012) from long GRBs.

4. CONCLUSION

GRB 140903A is characterized by its $\sim 10^6$ s radio afterglow emission. Some optical and X-ray afterglow data had also been recorded, rendering GRB 140903A as one of the few short events with afterglow emission in a very wide energy range (i.e., from radio to X-ray). We show in this work that the afterglow data can be self-consistently reproduced within the forward shock radiation scenario and at $t \leq 7 \times 10^3$ s an energy injection from the prolonged activity of the central engine is needed. The energy injection form suggests that the central engine is likely millisecond magnetar, similar to that needed for interpreting the X-ray flat segment of SGRB 051221A (Fan & Xu 2006). Such a result may suggest a relatively small total-gravitational-mass of the pre-merger binary system or a very hard equation of state of neutron stars that can yield the maximum gravitational mass $> 2.3 - 2.4 M_{\odot}$, this is because for the ten neutron-star binary systems observed in the Galaxy, their merger remnants will have a typical gravitational mass $\sim 2.3 - 2.4 M_{\odot}$, if no significant amount of material has been ejected (Fan et al. 2013). The inferred jet half-opening angle ~ 0.05 rad (2.9°) is very small, implying that hundreds more similar events took place in the local universe but in directions missing the earth.

Relative to the “frequent” detection of SGRB afterglow in X-rays and optical, the radio afterglow emission had just been detected in four events. To better understand the rare detection in radio bands, we carry out a statistical study to see whether there is a significant difference between the events with and without radio detections. The common features of these radio-detected GRBs are the relatively small redshifts and higher flux or flux density especially in optical band, implying that just the relatively nearby and energetic outflows are easier to give rise to detectable radio emission, consistent with the forward shock afterglow model.

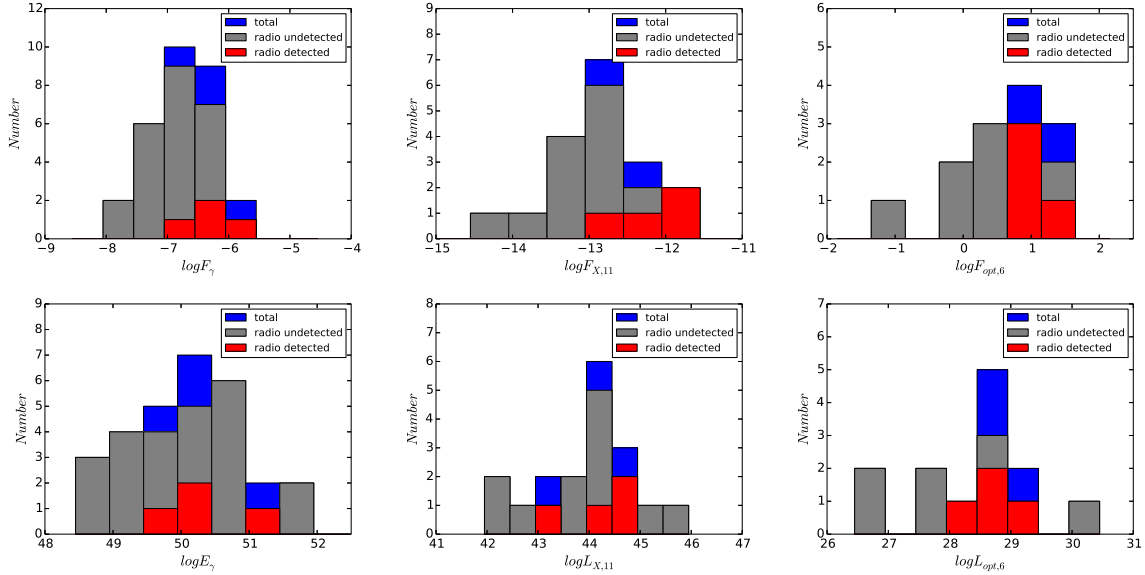


FIG. 4.— Distributions of F_γ , $F_{X,11}$, $F_{opt,6}$ and E_γ , $L_{X,11}$, $L_{opt,6}$. Red and gray color represent samples of GRBs with and without radio afterglow detections and blue represent total sample.

ACKNOWLEDGMENTS

We thank Dr. Y. Z. Fan for stimulating discussion. This work was supported in part by 973 Programme of China under grant 2014CB845800, National Natural Science Foundation of China under grants 11273063,

11361140349, 11433009, 11303098 and 11103084, the Chinese Academy of Sciences via the Strategic Priority Research Program (Grant No. XDB09000000) and the External Cooperation Program of BIC (No. 114332KYSB20160007).

REFERENCES

- Berger, E. 2014, *ARA&A*, 52, 43
 Berger, E., Fong, W., & Chornock, R. 2013, *ApJL*, 774, L23
 Berger, E., Price, P. A., Cenko, S. B., et al. 2005, *Natur*, 438, 988
 Burrows, D. N., Grupe, D., Capalbi, M., et al. 2006, *ApJ*, 653, 468
 Capone, J., Toy, V., Cenko, S. B. et al. 2014, *GCN Circ*, 16767
 Cenko, S. B. & Perley, D. A. 2014, *GCN Circ*, 16770
 Chandra, P., & Frail, D. A. 2012, *ApJ*, 746, 156
 Cohen, E., & Piran, T. 1999, *ApJ*, 518, 346
 Cucchiara, A., Cenko, S. B., Perley, D. A., Capone, J., & Toy, V. 2014, *GCN Circ*, 16774
 Cummings, J. R., Burrows, D. N., Evans, P. A. et al. 2014, *GCN Circ*, 16763
 Dai, Z. G., & Lu, T. 1998, *A&A*, 333, L87
 De Pasquale, M., Maselli, A. & Cummings, J. R. 2014, *GCN Circ*, 16767
 Dichiaro, S., Guidorzi, C., & Japelj, J. 2014, *GCN Circ*, 16781
 Eichler, D., Livio, M., Piran, T., & Schramm, D. N. 1989, *Natur*, 340, 126
 Fan, Y. Z., & Piran, T. 2006, *MNRAS*, 369, 197
 Fan, Y.-Z., Wu, X.-F., & Wei, D.-M. 2013, *Phys. Rev. D*, 88, 067304
 Fan, Y. Z., & Xu, D. 2006, *MNRAS*, 372, L19
 Fong, W. 2014, *GCN Circ*, 16777
 Fong, W., Berger, E., Margutti, R., & Zauderer, B. A. 2015, *ApJ*, 815, 102
 Fong, W., Berger, E., Metzger, B. D., et al. 2014, *ApJ*, 780, 118
 Fruchter, A. S. 2014, *GCN Circ*, 16776
 Gunn, J. E., & Ostriker, J. P. 1969, *Natur*, 221, 454
 Jin, Z. P., Hotokezaka, K., Li, X., et al. 2016, *NatCo*, 7, 12898
 Jin, Z. P., Li, X., Cano, Z., et al. 2015, *ApJL*, 811, L22
 Kasen, D., Badnell, N. R., & Barnes, J. 2013, *ApJ*, 774, 25
 Kennea, J. A. & Cummings, J. R. 2014, *GCN Circ*, 16764
 Kouveliotou, C., Meegan, C. A., Fishman, G. J., et al. 1993, *ApJL*, 413, L101
 Levan, A. J., Cenko, S. B., Cucchiara, A., & Perley, D. A. 2014, *GCN Circ*, 16774
 Li, L. X., & Paczyński, B. 1998, *ApJL*, 507, L59
 Li, X., Hu, Y. M., Fan, Y. Z., & Wei, D. M. 2016, *ApJ*, 827, 75
 Liang, E. W., Zhang, B. B., & Zhang, B. 2007, *ApJ*, 670, 565
 Nayana, A. J. & Poonam, C. 2014, *GCN Circ*, 16815
 Nousek, J. A., Kouveliotou, C., Grupe, D., et al. 2006, *ApJ*, 642, 389
 Pacini, F. 1967, *Natur*, 216, 567
 Palmer, D. M., Barthelmy, S. D., Baumgartner, W. H. et al. 2014, *GCN Circ*, 16768
 Panaitescu, A. 2006, *MNRAS*, 367, L42
 Panaitescu, A., Mészáros, P., Burrows, D., et al. 2006, *MNRAS*, 369, 2059
 Piran, T. 1999, *Phys. Rep.*, 314, 575
 Sakamoto, T., Troja, E., Gehrels, N. et al. 2014, *GCN Circ*, 16813
 Shapiro, S. L., & Teukolsky, S. A. 1983, *Research supported by the National Science Foundation*. New York, Wiley-Interscience, 1983, 663 p.,
 Soderberg, A. M., Berger, E., Kasliwal, M. et al. 2006, *ApJ*, 650, 261
 Tanvir, N. R., Levan, A. J., Fruchter, A. S., et al. 2013, *Natur*, 500, 547
 Troja, E., Sakamoto, T., Cenko, S. B., et al. 2016, *ApJ*, 827, 102
 Woosley, S. E., & Bloom, J. S. 2006, *ARA&A*, 44, 507
 Xu, D., Geier, S., Malesani, D. et al. 2014, *GCN Circ*, 16783
 Yang, B., Jin, Z. P., Li, X., et al. 2015, *NatCo*, 6, 7323
 Yost, S. A., Harrison, F. A., Sari, R., & Frail, D. A. 2003, *ApJ*, 597, 459
 Zhang, B., Fan, Y. Z., Dyks, J., et al. 2006, *ApJ*, 642, 354
 Zhang, S., Jin, Z. P., & Wei, D. M. 2015, *ApJ*, 798, 3
 Zhang, B., & Mészáros, P. 2001, *ApJL*, 552, L35
 Zhu, B., Zhang, F. W., Zhang, S., Jin, Z. P., & Wei, D. M. 2015, *A&A*, 576, A71